

1 Developing and diagnosing climate change indicators of regional aerosol optical properties

2 **Ryan C. Sullivan^{a+*}, Robert C. Levy^b, Arlindo M. da Silva^b, and Sara C. Pryor^{a,c}**

3 *a. Department of Earth and Atmospheric Sciences, Cornell University, Ithaca, NY*

4 *b. NASA Goddard Space Flight Center, Greenbelt, MD*

5 *c. Pervasive Technology Institute, Indiana University, Bloomington, IN*

6 *+ Now at Environmental Science Division, Argonne National Laboratory, Argonne, IL, USA*

7 **Corresponding author:*

8 *rcsullivan@anl.gov*

9

Accepted manuscript

10 Given the importance of aerosol particles to radiative transfer via aerosol-radiation
11 interactions, a methodology for tracking and diagnosing causes of temporal changes in regional-
12 scale aerosol populations is illustrated. The aerosol optical properties tracked include estimates
13 of total columnar burden (aerosol optical depth, AOD), dominant size mode (Ångström
14 exponent, AE), and relative magnitude of radiation scattering versus absorption (single scattering
15 albedo, SSA), along with metrics of the structure of the spatial field of these properties. Over
16 well-defined regions of North America, there are generally negative temporal trends in mean and
17 extreme AOD, and SSA. These are consistent with lower aerosol burdens and transition towards
18 a relatively absorbing aerosol, driven primarily by declining sulfur dioxide emissions.
19 Conversely, more remote regions are characterized by increasing mean and extreme AOD that is
20 attributed to increased local wildfire emissions and long-range (transcontinental) transport.
21 Regional and national reductions in anthropogenic emissions of aerosol precursors are leading to
22 declining spatial autocorrelation in the aerosol fields and increased importance of local
23 anthropogenic emissions in dictating aerosol burdens. However, synoptic types associated with
24 high aerosol burdens are intensifying (becoming more warm and humid), and thus changes in
25 synoptic meteorology may be offsetting aerosol burden reductions associated with emissions
26 legislation.

27 **1 Introduction**

28 Atmospheric aerosol particles (aerosols) impact biogeochemical cycles, human health,
29 and global and regional climate by scattering and absorbing radiation, acting as cloud
30 condensation nuclei or ice nucleating particles and altering cloud lifetimes and albedo, and
31 changing the atmospheric thermal structure and thus atmospheric stability (ref. 1 and references
32 therein). According to some estimates aerosol particles may have offset 0.9 Wm^{-2} (– 0.95 to +

33 0.05 Wm⁻² and – 1.2 to 0.0 Wm⁻² for aerosol-radiation (direct) and aerosol-cloud (indirect)
34 interactions, respectively) of the historical globally-averaged warming due to increased
35 greenhouse gas concentrations (2.26 to 3.40 Wm⁻²)². They have also been implicated as a major
36 source of regional and sub-regional variations in trends in near-surface temperature (e.g. in the
37 ‘warming hole’ of the central Great Plains)³⁻⁷.

38 Aerosol radiative forcing and climate impact are a function of the aerosol number
39 concentration, size distribution, and chemical composition, and remain a major source of
40 uncertainty in quantifying anthropogenic forcing of Earth’s climate². In contrast to well-mixed
41 greenhouse gases, as with other short-lived climate forcers, aerosols exhibit much higher
42 spatiotemporal variability. Local primary aerosol and precursor gas emissions have a major
43 impact on regional aerosol populations and thus climate impacts. Hence, quantifying the
44 radiative forcing is challenging and subject to large uncertainties. For example, during 1980 –
45 2009, the global mean annual aerosol optical depth (AOD), a measure of the extinction of
46 insolation by atmospheric aerosols and thus the reduction of radiation that reaches Earth’s
47 surface, was unchanged (i.e. remained within ± 0.01 of an estimated global average of ~ 0.15)⁸.
48 However, mean annual AOD decreased by up to 27% over parts of the U.S. and Europe due in
49 part to regulation of precursor and primary aerosol emissions, while mean annual AOD increased
50 by up to 22% over countries undergoing large economic development⁸⁻¹⁰. Following emission
51 reductions associated with air quality legislation (e.g., U.S. Clean Air Act)¹¹, near-surface fine
52 aerosol concentrations (PM_{2.5}, i.e. the mass concentration of aerosols with diameters less than 2.5
53 μm) decreased by 40% across the continental U.S. during this period⁸. This is consistent with a
54 38% decrease in modeled AOD from 1980 – 2006 (ref. 12), and $\sim 3\%$ yr⁻¹ decrease in summer

55 AOD over the eastern U.S. from 2001 – 2013 retrieved using satellite-based remote sensing (the
56 Multi-angle Imaging SpectroRadiometer (MISR))¹³.

57 In order to diagnose and track changes in key observable properties of the climate system
58 through time, a number of climate indicators (CI) have been developed and applied^{14,15}. Many
59 agencies that contribute to the U.S. Global Change Research Program (USGCRP) have
60 developed and applied CIs to document and track changes in the physical, chemical, and
61 anthropogenic (socio-economic) components of the climate system. The spatial or temporal
62 resolutions of CIs vary widely: Some are global in scale while others are regional, and while
63 some focus on the drivers of global change, others are more strongly focused on response
64 variables. Existing USGCRP CIs thus include: Regional and global air temperature,
65 precipitation, sea level, sea and land ice, and atmospheric concentrations of carbon dioxide,
66 methane, nitrogen oxides, and fluorinated gases¹⁴. Despite the role of aerosols in perturbing
67 regional climate, CIs of climate-relevant aerosol properties have yet to be developed¹⁵. Herein
68 we propose a suite of aerosol-CIs, and illustrate how they are derived and applied using regions
69 of the U.S. National Climate Assessment (NCA) program (Figure 1). We demonstrate how these
70 aerosol-CIs can be used to quantify variability and temporal trends in aerosol populations, and
71 attribute changes through time to specific drivers of aerosol variability: Gaseous precursor and
72 primary aerosol emissions, and meteorological conditions at the synoptic scale.

73 CIs must be predicated on high quality, uniform (gridded), and publically available data
74 with well-defined provenance and an expectation that the variables on which they are based will
75 continue to be measured into the future. Therefore observations, such as those from satellite- or
76 ground-based remote sensing, are not suitable for deriving aerosol-CIs due to spatiotemporal
77 discontinuities and a bias towards sampling cloud-free conditions¹⁶. Thus, we demonstrate the

78 benefit of deriving the proposed aerosol-CIs from the first homogeneous, gridded reanalysis
79 product that is constrained by satellite-based aerosol and meteorological measurements: Modern-
80 Era Retrospective Analysis for Research and Application, Version 2 (MERRA-2)^{17,18}. MERRA-2
81 provides gridded global hourly output of observable aerosol optical properties, including in
82 cloudy-sky scenes, with high fidelity when evaluated relative to independent (non-assimilated)
83 observations¹⁷.

84 Herein, we develop CIs of aspects of aerosol populations relevant for aerosol-radiation
85 interactions and climate at the regional scale, and using output from MERRA-2 apply the
86 aerosol-CIs to each NCA region (Figure 1) to provide an illustrative example of how they can be
87 used to quantify, characterize, and diagnose causes of historical trends in climate-relevant
88 aerosol properties. To the first order, three key properties of the aerosol population determine the
89 magnitude of the forcing due to aerosol-radiation interactions and thus the climate impact: Total
90 columnar burden, size of the aerosols, and their composition¹⁹. Thus the aerosol-CIs we propose
91 are based on: (1) AOD (550 nm), which is a measure of the column-integrated extinction of
92 radiation and is approximately proportional to the aerosol mass concentration. (2) Ångström
93 exponent (AE; 470 – 870 nm) which is qualitatively inversely proportional to particle size with a
94 secondary dependence on aerosol composition. (3) Single scattering albedo (SSA; 550 nm)
95 which is the ratio of scattering to total extinction, and describes the relative efficiency of
96 radiation scattering (leading to an increase in the global albedo and cooling) by aerosols to
97 radiation absorption (leading to atmospheric warming)². As aerosols potentially impact regional
98 scale climate in the U.S.^{4-7,20}, the proposed aerosol-CIs are designed to characterize and track
99 changes in regionally averaged mean conditions of these variables and their extreme values.
100 Further aerosol forcing must occur on relatively large scale for an appreciable climate impact,

101 and therefore the aerosol-CIs also characterize and track changes in the spatial scales of aerosol
102 features (both spatial autocorrelation and scales of coherence) (see Methods).

103 **2 Results**

104 **2.1 MERRA-2**

105 The release of the MERRA-2 dataset constitutes the first real opportunity to develop and
106 apply aerosol-CIs for the U.S. NCA regions, or any other part of the globe. Aerosol properties in
107 the MERRA-2 reanalysis product are derived in part based on assimilation of AOD at 550 nm
108 derived from remotely sensed properties such as spectral reflectances, solar and instrument
109 geometry, cloud cover, and surface features into the Goddard Earth Observing System, version 5
110 (GEOS-5) model¹⁸ (see Methods). MERRA-2 has been subject to extensive evaluation relative to
111 independent observations, and thus only limited additional evaluation was undertaken as part of
112 this study and is focused on evaluation of the joint probabilities of the key variables considered
113 herein: AOD, and AE and SSA relative to those from ground-based measurements of columnar
114 aerosol properties from AEROSOL ROBOTIC NETWORK (AERONET) stations²¹ (see Methods;
115 Figure S1).

116 **2.2 Development of aerosol-CIs**

117 AOD, AE, and SSA describe key aspects of aerosol particle populations that have
118 greatest relevance to direct radiative forcing via aerosol-radiation interactions. Accordingly our
119 proposed aerosol-CIs are based on daily values derived by averaging in space (i.e. over the NCA
120 regional definitions shown in Figure 1) and time, the hourly estimates of total column
121 (anthropogenic and natural) AOD, AE, and SSA. The aerosol-CIs are thus daily mean AOD, AE,
122 SSA and extreme (90th percentile (P90 AOD)) AOD, along with two key metrics of the spatial
123 patterns of these variables: The daily global spatial autocorrelation value (characterized using

124 Moran's-I²²; AOD-I, AE-I, SSA-I) and the range of spatial coherence as derived using
125 semivariograms²³ of daily AOD, AE, and SSA fields within each region (AOD-SC, AE-SC,
126 SSA-SC) (Figure 2). Moran's-I quantifies the degree of spatial clustering in the field and
127 semivariograms quantify the distance at which two locations become independent. These ten
128 aerosol-CIs are designed to track evolution of regional aerosol populations in terms of the overall
129 aerosol columnar burden, average aerosol diameter, relative proportions of absorbing versus
130 scattering aerosols, and the regional consistency of the spatial patterns of those properties.

131 Each aerosol-CI contains unique information about regional aerosol properties that have
132 different implications for direct radiative forcing. These CIs also exhibit intra- and inter-annual
133 variability and trends that are not consistent across indicators indicating the utility of all of the
134 proposed aerosol-CIs to trend diagnostic and attribution analyses (Figure 2). To detect potential
135 redundancy in the aerosol-CIs, a principal component analysis (PCA) was conducted. Although
136 the aerosol-CIs exhibit co-linearity, the aerosol-CIs tend to fall primarily on orthogonal principal
137 components, and the PCA indicates that there is not a coherent, physically consistent set of
138 synthetic, comprehensive indicators across the different regions. Further, for a true climate
139 impact to be realized, aerosol radiative forcing must be expressed over a large area. Thus, there
140 is a need to understand and quantify the degree to which climate-relevant aspects of aerosol
141 populations are regionally coherent.

142 **2.3 Application of the aerosol-CIs to regions of the U.S. NCA**

143 Consistent with previous research, mean and extreme (P90) AOD declined in virtually all
144 NCA regions over the period 2000 – 2015 (Figure 2). Significant (hereafter $\alpha = 0.05$, unless
145 otherwise indicated) decreases are observed in five regions: the lower Great Plains (GPI),
146 Midwest (MW), Southeast (SE), Northeast (NE), and Alaska (AK), but increased mean and

147 extreme AOD is observed for the Northwest (NW), and there was no change in the Southwest
148 (SW) and upper Great Plains (GPu). To examine trends in AOD, AE, and SSA across their
149 respective probability distributions (c.f. to only mean and extreme values in the CIs), Figure 3a-c
150 shows the cumulative distribution functions (cdf) in each region for 2000 – 2015, as well as, the
151 deviation from the mean cdf for each individual year. The direction of change and the presence
152 of significant trends are consistent for mean and extreme (P90) AOD in all regions, but the
153 magnitude of the change is larger for extreme AOD, indicating a narrowing of the AOD
154 probability distributions (Figure 3a). Significant regional AOD trends are $\sim 1\% \text{ year}^{-1}$, while the
155 magnitude of the extreme AOD trends are $1.2 - 1.4\% \text{ year}^{-1}$ in regions of decreasing AOD and
156 $1.9\% \text{ year}^{-1}$ for the NW (Figures 2, 3, and S2). There is marked seasonality in some regions in
157 terms of both the magnitude of and temporal trends in the aerosol-CIs. For example, extreme
158 (P90) AOD significantly decreased in summer (the season of highest historical values), spring,
159 and fall in NE, summer and fall in SE and MW (p-value = 0.06 for MW summer), and during fall
160 in GPI. Conversely P90 AOD increased in summer and fall in NW (Figure 3d).

161 The key utility of including two indices of spatial structure of the fields is illustrated by
162 the divergent trends in these two aerosol-CIs. All regions exhibit decreased AOD spatial
163 autocorrelation (AOD-I), but increased AOD spatial coherence (AOD-SC) is observed over the
164 NW, GPI, MW, SE, and AK, and decreased AOD-SC is observed in the SW (p-value = 0.07),
165 GPu (p-value = 0.15), and NE (Figures 2 and S3). Causes of these differences and the inter-
166 annual variability in the aerosol-CI trends are discussed below.

167 Mean AE significantly increased across all eight regions, indicating a decrease in mean
168 particle size (Figures 2 and S2). This shift to higher AE is observed across the probability
169 distribution, implying a shift in fine mode aerosols to smaller sizes, as opposed to a relative

170 increase in fine versus coarse mode aerosols (Figure 3b). However, trends in the spatial metrics
171 of AE are not uniform across the regions. Significant negative trends in AE-I are observed in
172 NW, SW, GPU, MW, and AK (Figures 2 and S3), but only two regions exhibited significant
173 changes in AE-SC and they showed different signs (increased in SW and decreased in NE).
174 Thus, there is evidence that as the aerosol populations are, on average, decreasing in diameter at
175 the regional scale, but there remain sub-regions within many of the NCA regions with high
176 coarse mode concentrations (e.g., across all days, 50 % of grid cells have $AE \leq 1.2$ in the NW,
177 SW, and GPU; Figure 3b), possibly due to wind-blown dust events²⁴.

178 Mean SSA and SSA-SC decreases are observed in all eight regions (Figure 2). There are
179 also decreases in SSA-I for all regions except SE where there were significant increases in SSA-
180 I, although the significance of the trend is lower in GPU (p -value = 0.06) and AK (p -value =
181 0.16). It is noted that SSA is determined by the aerosol composition and the dynamic range of
182 SSA in MERRA-2 is lower than observations^{17,25} (Figure S1); therefore the aerosol-CIs that
183 relate to SSA must be viewed with caution in the current reanalysis product. However, these
184 trends are consistent with a tendency towards a relatively more absorbing aerosol, thus reducing
185 the net cooling from aerosols. Further, the trends in SSA-I and SSA-SC imply aerosol
186 populations are becoming more spatially heterogeneous in terms of the relative contribution of
187 absorption to total radiative extinction.

188 When applied to the U.S. NCA regions, the aerosol-CIs thus indicate substantial
189 evolution of aerosol populations through time in ways that are relevant to regional climate
190 forcing. Overall aerosol burdens have declined (2000 – 2015) and on average aerosol populations
191 have changed to become more dominated by smaller diameter and more absorbing aerosols.

192 They are also evolving in a way that causes a decrease in spatial autocorrelation, but increases in
193 spatial coherence.

194 **2.4 Attribution of temporal trends in the aerosol-CIs**

195 Attribution of observed trends in the aerosol-CIs, particularly deconvoluting changes
196 resulting from changing anthropogenic emissions, natural emissions, and atmospheric conditions
197 is critical to demonstrating the effectiveness of emission reduction policies, exploring and
198 prioritizing potential climate change mitigation strategies, and making projections of possible
199 future values of the aerosol-CIs. Thus, the aerosol-CIs for the NCA regions are examined below
200 in the context of these key drivers of aerosol populations.

201 Aerosol-climate interactions are reciprocal. Aerosols are a major driver of climate
202 variability and change, but equally changes in climate alter aerosol concentrations and
203 composition²⁶⁻²⁸. Further, previous research has illustrated a key role of synoptic scale
204 meteorological conditions in determining regional aerosol concentrations under the
205 current^{29,30,3,31} and possible future climate^{32,33}. Consistent with that research, in each of the NCA
206 regions, a number of synoptic types (i.e. repeated meteorological patterns) derived in a PCA of
207 MERRA-2 meteorological output are associated with 10 – 20 % AOD anomalies (positive and
208 negative from the mean) (Figure 4). The link to meteorological conditions at the synoptic scale is
209 less pronounced for AE (the anomalies are < 10 %) and it appears SSA is relatively insensitive of
210 the prevailing meteorological conditions (no synoptic type had a regionally average SSA
211 anomaly of > 2%). This finding re-emphasizes the complexity of aerosol populations and their
212 related climate forcing, and highlights the importance of having multiple aerosol-CIs in order to
213 fully characterize changes in climate-relevant aerosol properties.

214 Over all regions, synoptic types characterized by cooler (or milder) and drier conditions
215 are associated with lower AOD. Conversely, anomalously high AOD is associated with warm
216 and/or humid synoptic types, consistent with enhanced AOD under stagnant flow²⁹ and aerosol
217 growth by water uptake³⁴. Over the northern and western regions of the contiguous U.S. (NW,
218 SW, GPU, MW) southwesterly geostrophic flow is typically associated with positive anomalies
219 in both mean and extreme AOD, while northwesterly flow is associated with negative anomalies
220 in mean and extreme AOD (Figure 4). Anomalously low AE in virtually all regions is often
221 associated with cool, dry synoptic conditions, consistent with an increase in dust loading during
222 dry conditions²⁴. Conversely, high AE is associated with warm, humid conditions at the synoptic
223 scale consistent with predominance of hygroscopic secondary aerosols.

224 Consistent with prior research that has indicated changes in global and regional
225 temperature and humidity are likely to result in changing characteristics of the synoptic
226 types^{29,35}, the majority of synoptic types associated with large positive AOD anomalies in each
227 region exhibit a significant positive trend in PC scores. Conversely, synoptic types associated
228 with negative AOD anomalies exhibited trends that are divided between increasing and
229 decreasing trends (Figure 4). While there is evidence that some cool, dry days are also becoming
230 cooler and drier, the dominant signal in this analysis is thus that synoptic types associated with
231 elevated AOD are evolving to become more intense, i.e. warm, humid days becoming warmer
232 and more humid. These changes in the synoptic-scale climate may thus partially offset emissions
233 reductions^{26,28}. While the intensity of the synoptic types has changed, the frequencies of
234 individual synoptic types over each region do not exhibit significant temporal trends over the
235 period 2000 – 2015.

236 Consistent with policy enacted under the U.S. Clean Air Act that has resulted in declining
237 anthropogenic pollutant emissions over the study period, regionally integrated emissions of key
238 aerosol precursor species, sulfur dioxide (SO₂) and nitrogen oxides (NO_x), exhibit a significant
239 negative trend for all eight NCA regions over the period 2000 – 2015. Further ammonia (NH₃)
240 emissions exhibit a negative trend in all regions except the MW and NE, and volatile organic
241 compounds (VOC) emissions exhibit a negative trend in all regions except the NW and SE
242 (Figure 5)³⁶. Consistent with this, mean and extreme AOD significantly decreased in GPI, MW,
243 SE, and NE, and seasonal extreme AOD decreased in the fall in GPI, summer and fall in MW
244 and SE, and spring, summer, and fall in NE. The overall tendencies in aerosol-CIs, including the
245 significant decrease in mean and extreme AOD over GPI, MW, SE, and NE, are thus consistent
246 with a decrease in sulfate aerosol abundance due to the reduction in SO₂ emissions (e.g.,
247 correlation coefficients between annual SO₂ emissions and extreme summer (except GPI) and
248 fall AOD are > 0.57 over these regions). Congruent with this decline in SO₂ emissions, the
249 annual deviations from the overall cumulative distribution functions (cdf) imply that almost the
250 entire probability distribution of AOD has shown a shift towards lower values (Figure 3a).
251 Further, because sulfate has a high SSA (near unity)³⁷, a reduction in secondary sulfate aerosol
252 would also contribute to the observed decline in regionally-averaged SSA. Reduced production
253 of sulfuric acid may also lead to a reduction in mean aerosol diameter, implied by the increase in
254 AE, due to a reduction in condensational growth. While historic trends in black carbon (BC)
255 emissions are highly uncertain (e.g., from biomass burning), it is estimated emissions from
256 mobile sources, the largest BC source in the U.S., decreased by 32 % from 1990 – 2005 (ref. 38).
257 Further, BC only contributes to ~ 4 % of global AOD¹⁸. Thus changes in SSA are likely not due
258 to changes in anthropogenic BC emissions. Secondary organic aerosols are also a substantial

259 component of aerosol mass and AOD over much of the eastern U.S.³⁹. Thus an additional
260 contributory factor to declining AOD in these regions is the reduction in anthropogenic VOC
261 emissions and secondary organic aerosol formation. Accordingly, the correlation coefficients
262 between annual VOC emissions and extreme summer and fall AOD in the NE and MW are >
263 0.61. Thus, consistent with prior research, historical temporal trends of AOD across much of the
264 contiguous U.S. are strongly responsive to emission reductions associated with the Clean Air
265 Act.

266 Despite reductions in anthropogenic aerosol precursor gas emissions, it is worthy of note
267 that primary aerosol emissions exhibit a significant trend only in the NW, GPU, and MW (Figure
268 5), and that biogenic VOC, dust, and wildfire emissions exert a substantial impact on aerosol
269 burdens and optical properties^{40,41}. For example, there is a clear peak in extreme AOD in the
270 spring of 2011 in the GPI, MW, and SE when wildfire burned area in the GPI was approximately
271 four times greater than any other year (Figures 3 and 5). In the GPI, the lack of association (i.e.
272 lower correlation coefficients) between annual anthropogenic emissions and extreme AOD in
273 three of the four climatological seasons and the observed decreased SSA may also be in part due
274 to increased abundance of dust aerosols, consistent with remote sensing measurements that
275 indicate increased dust-related absorption aerosol optical depth (AAOD) over the central U.S.²⁴.
276 The declining trend in AOD in AK is also not very strongly linked to changes in anthropogenic
277 emissions, but there is a significant positive association between extreme summer AOD and
278 wildfire burned area ($r = 0.96$). This is clearly evident in 2004, 2009, and 2015, when positive
279 excursions in monthly burned area (Figure 5) coincide with spikes in summer extreme AOD
280 (Figure 2).

281 Only the NW region exhibits a significant positive trend in annual mean AOD, with
282 extreme AOD increasing in the summer and fall (Figure 2 and 3). This is despite declines in
283 regional anthropogenic emissions (Figure 5), and may reflect confounding influences from
284 increased wildfires (seasonal burned area and extreme AOD in summer and fall exhibit co-
285 variability with $r = 0.53$ and 0.75 , respectively) and long-range transport. For example, Siberian
286 fires in the summer of 2012 impacted air quality in the Pacific NW⁴¹, and are evident in high P90
287 AOD during the 2012 summer and fall (Figure 2).

288 The decrease in the spatial autocorrelation in AOD (Figures 2 and S3) along with the
289 decreased anthropogenic aerosol precursor emissions in each region (Figure 5) indicates an
290 increasing influence of local sources on sub-regional aerosol concentrations and thus increased
291 grid cell-to-grid cell variability in aerosol populations. Conversely, scales of spatial coherence
292 (distance at which grid cells become independent) are increasing, which may be linked to
293 changes in synoptic scale conditions (Figure 4). High and low AOD are generally associated
294 with warm, humid and cool, dry conditions, respectively. The positive trend in PC scores for
295 synoptic types associated with high positive AOD anomalies indicate a tendency towards
296 intensification of meteorological conditions associated with large direct aerosol radiative forcing
297 that may be offsetting some of the effects of emission controls. As climate conditions continue to
298 evolve, this highlights the critical need to better understand the feedbacks between climate and
299 aerosol populations.

300 **3 Discussion**

301 Use of climate indicators to represent key components of the climate system is an
302 increasing focus of the U.S. NCA. For this reason, we advocate that aerosol-CIs are urgently
303 needed to track a key aspect of the radiation balance of Earth, air quality, and biogeochemical

304 cycles, and that aerosol-CIs should be generated and interpreted at the regional scale. The
305 guidance for developing CIs is that they should be relatively straightforward to compute and
306 readily evaluated in both the contemporary and possible future climate. Thus, the aerosol-CIs we
307 propose can be readily derived for any gridded data set and therefore can be applied to any
308 region using current and future generation reanalysis products and/or output from regional and
309 climate models.

310 The aerosol-CIs presented herein are designed to be useful in tracking changes in climate
311 relevant aspects of the aerosol population and to assist in diagnosing the causes of changes in
312 aerosol populations at the regional scale. Their utility in the former regard is illustrated by
313 application to the NCA regions, and specifically the finding that mean and extreme AOD and
314 SSA is declining and AE is increasing over most of the U.S. consistent with a tendency towards
315 lower aerosol burdens that are increasingly dominated by smaller diameter and relatively more
316 absorbing aerosols. This implies a decline in the degree to which aerosols have offset greenhouse
317 gas related warming of the climate over much of the contiguous U.S.

318 The aerosol-CIs are also defined using two geospatial metrics: Spatial correlation and
319 spatial coherence. The former (Moran's I) characterizes normalized co-variability and is a
320 measure of the degree to which daily fields of AOD, AE, and SSA exhibit spatial clustering. The
321 latter is a measure of the distance (range in the semivariogram) at which spatial fields become
322 independent, and thus the extent to which the aerosol forcing can impact regional climate. The
323 utility of these two spatial metrics in terms of diagnosing causes of changes in aerosol
324 populations at the regional level is also indicated by the presence of divergent trends in AOD-I
325 and AOD-SC in the NCA regions. These findings imply a tendency towards more grid cell-to-
326 grid cell variability in aerosol populations, due to declining regional precursor and aerosol

327 emissions leading to an increase in the relative importance of local emissions, within larger areas
328 of increased spatial coherence (i.e. large range values from the semivariograms) in part due to an
329 increase in the intensity of the predominant modes of synoptic scale meteorology.

330 Future work is needed to examine aerosol trends in global regions outside of the U.S. that
331 are characterized by markedly different emissions and climate trends. Additionally, analyses of
332 reanalysis products are only as good as the assimilation data and model used to develop the
333 product. Thus the CIs should be applied to future reanalysis products that assimilate improved
334 bias-correction assimilated data, data from additional, recently launched sensors, and more
335 sophisticated model frameworks with improve aerosol treatment and emissions inventories.

336 **4 Methods**

337 **4.1 MERRA-2**

338 MERRA-2 is derived using assimilation of both meteorological and aerosol observations
339 every 6 and 3 hours, respectively, into the Goddard Earth Observing System, version 5 (GEOS-
340 5) model¹⁸. It provides hourly, global gridded output of meteorological variables and aerosol
341 optical properties including AOD, AE, and aerosol scattering extinction at 0.625° by 0.5°
342 resolution. The aerosol characteristics are constrained using a wide suite of remote sensing
343 products. For example, AOD at 550 nm is derived from Moderate Resolution Imaging
344 Spectroradiometer (MODIS) measurements on both the Terra and Aqua satellites (Collection
345 5)⁴² of reflectances, solar and instrument geometry, cloud cover, and surface features¹⁸ using a
346 neural network retrieval (NNR) trained using AERONET measurements. A similar approach is
347 used to assimilate Advanced Very High Resolution Radiometer (AVHRR)⁴³ measurements of
348 radiances, total precipitable water, wind speed, and solar and instrument geometry trained to the
349 MODIS NNR. MISR AOD is assimilated only over bright surfaces⁴⁴, and ground-based AOD

350 measurements from the AERONET²¹ are assimilated after 1999. As the density of assimilated
351 aerosol optical properties and meteorological measurements increases greatly after 2000 (ref.
352 18,45), the analysis presented here is limited to 2000 – 2015.

353 MERRA-2 output includes surface short- and longwave radiation fluxes, with and
354 without clouds, and with and without aerosols, which could be used to estimate aerosol radiative
355 forcing. However these properties are dependent on the radiative transfer model and treatment of
356 aerosol optical properties within the reanalysis model. Thus, herein we only use observable
357 variables that are more closely tied to the assimilated data.

358 MERRA-2 aerosol properties that are not directly assimilated have been compared to,
359 and found to be in reasonable agreement with, satellite-based radiometric measurements. For
360 example, monthly mean biases relative to the Ozone Monitoring Instrument (OMI) retrieved
361 absorption aerosol optical depth (AAOD) are typically $< |0.02|$ over the NCA regions, and
362 MERRA-2 reproduces the aerosol vertical profile (e.g., height of peak attenuation backscatter)
363 retrieved from the Cloud-Aerosol Lidar with Orthogonal Polarization (CALIOP) over the
364 continental U.S. (CONUS)¹⁷. MERRA-2 has also been evaluated relative to near-surface
365 measurements of PM_{2.5}. Again the results indicate a relatively high degree of consistency with
366 independent observations. For most months across the CONUS, MERRA-2 PM_{2.5} is within one
367 standard deviation of the in situ measurements, although there is an underestimation of winter
368 PM_{2.5} concentrations over the northwest and northeast U.S., potentially due to lack of nitrate
369 aerosols in MERRA-2 (ref. 17).

370 Our analysis of the joint probabilities of AOD, and AE and SSA from MERRA-2 relative
371 to AERONET, indicate good agreement, although MERRA-2 underestimates the dynamic range
372 of AE and SSA (Figure S1). Such underestimation is common when comparing gridded aerosol

373 datasets that represent area means ($\sim 2,500 \text{ m}^2$ for MERRA-2) versus in situ observations such as
374 the pseudo-point measurements from AERONET. MERRA-2 reproduces the observed region-to-
375 region variability in aerosol radiative properties and the MERRA-2 versus AERONET
376 differences tend to be smaller than region-to-region differences (Figure S1).

377 Physical variables from MERRA-2 used here within the synoptic-scale meteorological
378 classification have also been extensively evaluated in the previous MERRA release. For
379 example, the mean residual between MERRA and observations is $< 0.5 \text{ hPa}$ for Northern
380 hemisphere surface pressures and $\sim < 1\text{K}$ for temperature through the depth of the atmosphere
381 relative to radiosonde measurements⁴⁶. Since the original MERRA reanalysis, the GEOS model
382 has been further updated to reduce erroneous trends and discontinuities deriving from breaks in
383 assimilated measurements, and to reduce biases in the water cycle. For all regions in the
384 CONUS, MERRA-2 mean summer precipitation is within $\sim 0.5 \text{ mm day}^{-1}$ ($\sim 0.1 - 0.2 \text{ mm day}^{-1}$
385 averaged across the CONUS) of surface rain gauge measurements and exhibits an anomaly
386 correlation of ~ 0.9 for 1980 – 2011 (ref. 47).

387 The advantages of using the MERRA-2 product for development of aerosol-CIs are
388 manifold. These include use of a consistent data assimilation system for the entire period of
389 record. However, any reanalysis system is subject to inherent uncertainties due either to
390 assimilated variables and/or the model system. For example, an artificial trend exists in Terra
391 radiances assimilated into MERRA-2, which may confound the trend analysis presented herein.
392 Thus trends identified here should be further validated with future MERRA releases in which
393 this trend is corrected and/or with other aerosol reanalysis products as they become available.

394 **4.2 Wildfire and anthropogenic emissions**

395 Estimates of wildfire occurrence and spatial extent used herein to diagnose trends in the
396 aerosol-CIs derive from the Global Fire Emissions Database (GFED4) monthly burned area
397 product. GFED4 provides monthly estimates of hectares of burned area on a 0.25° grid derived
398 from the MODIS (Collection 5.1) monthly burned area product⁴⁸.

399 Annual estimates of anthropogenic emissions of carbon monoxide (CO), NH₃, NO_x,
400 PM₁₀, PM_{2.5}, SO₂, and VOCs are also used in attribution of changes in the aerosol-CIs. These
401 estimates are accumulated for all states within each of the NCA regions and derive from the
402 EPA's state level National Emissions Inventory (NEI)³⁶. It is noted that there is inherent
403 uncertainty in emissions estimates due to spatiotemporal variability in emission sources,
404 measurement and sampling errors, and the simplification of modeled emissions processes. For
405 example, SO₂ emissions rely on the sulfur content of the combustible material, biogenic
406 emissions vary with environmental conditions, and NH₃ emissions lack wide-spread regulatory
407 restrictions and ambient NH₃ measurements are scarce^{49,50}. Additionally, MERRA-2 aerosol
408 speciation depends, in part, on the magnitude of prescribed emissions, which do not evolve (i.e.
409 persistency is assumed) during the later years of the study period¹⁸. Despite these uncertainties,
410 measurements of species important for secondary aerosol formation, e.g. SO₂, suggest that trends
411 in emissions are robust^{13,51}.

412 **4.3 Statistical methods used to derive and interpret the aerosol-CIs**

413 The aerosol-CIs we propose quantify the regionally-averaged mean AOD, AE, and SSA;
414 extreme (90th percentile) AOD; and two geostatistical metrics of spatial autocorrelation and
415 spatial coherence of AOD, AE, and SSA. The regionally averaged mean and P90 values are
416 computed from hourly output that are aggregated in space and time to generate daily mean

417 values for each property that then comprise each CI. While a spatial mean is used here, previous
 418 work indicates that spatiotemporal averages are sensitive to averaging methodology⁵²,
 419 particularly for variables such as AE⁵³. The spatial autocorrelation (AOD-I, AE-I, SSA-I) and
 420 spatial coherence (AOD-SC, AE-SC, SSA-SC) statistics are computed from the daily mean of
 421 the hourly output for each grid cell.

422 The global spatial autocorrelation for each region and aerosol parameter is computed at
 423 the daily timescale and quantified using Moran's I²²:

$$424 \quad I = \frac{N}{\sum_{i=1}^N \sum_{j=1}^N w_{ij}} \frac{\sum_{i=1}^N \sum_{j=1}^N w_{ij} (X_i - \bar{X})(X_j - \bar{X})}{\sum_{i=1}^N (X_i - \bar{X})^2} \dots (1)$$

$$425 \quad w_{ij} = \frac{1}{D_{ij}^2} \frac{1}{\sum_{i=1}^N \sum_{j=1}^N \frac{1}{D_{ij}^2}} \dots (2)$$

426 where N is the number of grid cells, w_{ij} is the weight for grid cells i and j, X_i is the daily mean
 427 value (AOD, AE, or SSA) at grid cell i, \bar{X} is the mean of the daily means for all grid cells, and D_{ij}
 428 is the great circle distance between the centroid of grid cell i and j. Values approaching 1 and -1
 429 indicate positive and negative spatial autocorrelation, respectively, while 0 indicates a random
 430 spatial field. Significance for rejecting the null hypothesis of no spatial autocorrelation is
 431 determined by calculating a z-score for each I:

$$432 \quad Z = \frac{I - E(I)}{\text{Var}(I)} \dots (3)$$

$$433 \quad E(I) = -\frac{1}{N-1} \dots (4)$$

$$434 \quad \text{Var}(I) = \frac{NS_4 - S_3S_5}{(N-1)(N-2)(N-3) \left(\sum_{i=1}^N \sum_{j=1}^N w_{ij} \right)^2} - E(I)^2 \dots (5)$$

$$435 \quad S_1 = \frac{1}{2} \sum_{i=1}^N \sum_{j=1}^N (2w_{ij})^2 \dots (6)$$

436
$$S_2 = \sum_{i=1}^N \left(2 \sum_{j=1}^{N, i \neq j} w_{ij} \right)^2 \dots (7)$$

437
$$S_3 = \frac{\frac{1}{N} \sum_{i=1}^N (X_i - \bar{X})^4}{\left(\frac{1}{N} \sum_{i=1}^N (X_i - \bar{X})^2 \right)^2} \dots (8)$$

438
$$S_4 = (N^2 - 3N + 3)S_1 - NS_2 + 3 \left(\sum_{i=1}^N \sum_{j=1}^{N, i \neq j} w_{ij} \right)^2 \dots (9)$$

439
$$S_5 = (N^2 - N)S_1 - 2NS_2 + 6 \left(\sum_{i=1}^N \sum_{j=1}^{N, i \neq j} w_{ij} \right)^2 \dots (10)$$

440 The spatial coherence of each variable in each region is computed using semivariograms which
 441 describe the semivariance as a function of separation distance between all grid cell pairs²³:

442
$$\gamma(h) = \frac{\sum_{i=1}^{N, i \in Q} \sum_{j=1}^{N, D_{ij} \in h} [X_i - X_j]^2}{N(h) \times |Q|} \dots (11)$$

443 Where $N(h)$ is the number of grid cell pairs that are separated by a great circle distance of h , X_i
 444 and X_j are the daily mean values (AOD, AE, or SSA) at grid cells i and j , respectively, h is a bin
 445 range of separation distances, and Q is the set of all grid cells not within three grid cells of the
 446 domain border. The empirical semivariogram fit, $\gamma(h)$, is binned in 100 km increments (i.e.
 447 $\gamma(1 - 100 \text{ km})$ includes all grid cell pairs separated by 1 – 100 km). An exponential fit is used
 448 to model $\gamma(h)$ assuming an exponential decay in correlation with distance and for physical
 449 interpretability of the model^{53,54}.

450
$$\gamma'(h) = C_n + C_p \left(1 - e^{-\frac{3h}{a}} \right) \dots (12)$$

451 Where $\gamma'(h)$ is the exponential model fit; C_n is the nugget describing the semivariance at zero
 452 spatial lag, resulting from variability at scales below data resolution⁵⁴; C_p is the partial sill, where
 453 the sill, $C_n + C_p$, is the semivariance as $h \rightarrow \infty$; and a is the range or distance at which 95% of the

454 sill is reached, indicating the distance at which two locations are no longer correlated. $\gamma(h)$ is
 455 calculated for each day, and $\gamma'(h)$ is fit to the mean $\gamma(h)$ for all days in each season⁵³. For the
 456 CIs to be tracked through time, a single daily quantity is required. Thus, the daily “scale of
 457 spatial coherence”, SC, is herein defined as the minimum h where $\gamma(h) > 0.75 \times C_p(a_s)$, where
 458 $C_p(a_s)$ is the partial sill for that season. While the spatial structure of the AOD and SSA fields is
 459 well represented by an exponential model, within the spatial extent of the individual regions AE
 460 semivariance tends to increase linearly with distance leading to higher uncertainty in a range
 461 determined using the exponential semivariogram model.

462 Temporal trends in the aerosol-CIs are quantified and the significance determined using
 463 Kendall’s tau-b (τ_b) rank coefficient⁵⁵. τ_b is calculated by comparing all pairs of observations,
 464 $\{(t_i, X_i), (t_j, X_j)\}$ where X_i and X_j are the variable (AOD, AE, SSA) at time t_i and t_j , respectively:

$$465 \quad \tau_b = \frac{C - D}{\sqrt{\left[\frac{N(N-1)}{2} - \sum_{i=1}^N \frac{tx_i(tx_i-1)}{2}\right] \left[\frac{N(N-1)}{2} - \sum_{i=1}^N \frac{tt_i(tt_i-1)}{2}\right]}} \dots (13)$$

$$466 \quad C - D = \sum_{i=1}^N \sum_{j=i+1}^N \begin{cases} \text{if } [\text{sign}((X_i - X_j)(t_i - t_j)) > 0] = 1 \\ \text{if } [\text{sign}((X_i - X_j)(t_i - t_j)) < 0] = -1 \\ \text{else} = 0 \end{cases} \dots (14)$$

$$467 \quad tx_i = |X : X = X_i| \dots (15)$$

$$468 \quad tt_i = |t : t = t_i| \dots (16)$$

469 where N is the number of observations. $\tau_b > 0$ indicates a positive trend and $\tau_b < 0$ indicates a
 470 negative trend. The significance of the trend is quantified using z-scores⁵⁶:

$$471 \quad Z = \frac{C - D}{\sqrt{\frac{v_0 - v_x - v_t}{18} + v_1 + v_2}} \dots (17)$$

$$472 \quad v_0 = N(N - 1)(2N + 5) \dots (18)$$

473
$$v_x = \sum_{i=1}^N tx_i(tx_i - 1)(2tx_i + 5) \dots (19)$$

474
$$v_t = \sum_{i=1}^N tt_i(tt_i - 1)(2tt_i + 5) \dots (20)$$

475
$$v_1 = \frac{\sum_{i=1}^N tx_i(tx_i - 1) \sum_{j=1}^N tt_j(tt_j - 1)}{2N(N - 1)} \dots (21)$$

476
$$v_2 = \frac{\sum_{i=1}^N tx_i(tx_i - 1)(tx_i - 2) \sum_{j=1}^N tt_j(tt_j - 1)(tt_j - 2)}{9N(N - 1)(N - 2)} (22)$$

477 The slope of the trends, in terms of percentage change per year, is estimated to be the slope of a
 478 linear regression fit to the CIs' time series.

479 It is hypothesized that changes in anthropogenic and natural precursor and primary
 480 aerosol emissions will be associated with changes in the aerosol populations. The significance of
 481 this association is quantified using the Pearson's r correlation coefficient.

482 Prior research indicates that synoptic meteorological conditions are also a key control of
 483 aerosol concentrations^{29,30}. Thus, PCA is used to derive a daily synoptic classification for all
 484 days in the study period and investigate the interaction between synoptic conditions and aerosol
 485 properties, and to determine the impact of meteorology on the CIs trends. Predictors used in the
 486 PCA are air temperature and specific humidity at 700 hPa plus 500 hPa geopotential heights
 487 from MERRA-2. The number of PCs to retain for each region was determined using a scree
 488 test⁵⁷ and the retained factors are rotated using a Varimax rotation⁵⁸. Between six and nine
 489 components (i.e. unique synoptic types) were retained for each of the eight NCA regions. The PC
 490 scores for each day (i.e. similarity to the major modes of variability as characterized by the PCs)
 491 are used to track changes in the frequency of each synoptic type (i.e. counts of days with highest
 492 similarity to each of the modes) and the intensity of the types (i.e. the magnitude of the scores for
 493 each PC). The mean anomaly of each aerosol-CI on all days classified by each synoptic type,

494 calculated relative to the mean aerosol-CI computed for all days, is used to illustrate the
495 importance of meteorological conditions at the synoptic (regional) scale in determining aerosol
496 properties.

497 **4.4 Data availability**

498 MERRA-2 data is available from the Goddard Earth Science Data and Information
499 Services Center (<https://disc.sci.gsfc.nasa.gov/>), AERONET data is available from
500 <https://aeronet.gsfc.nasa.gov/>, GFED4 is available from <http://www.globalfiredata.org/>, and NEI
501 is available from https://www.epa.gov/sites/production/files/2016-12/state_tier1_90-16.xls.

502 **5 References**

- 503 1. Yu, H. *et al.* A review of measurement-based assessments of the aerosol direct radiative
504 effect and forcing. *Atmos. Chem. Phys.* **6**, 613–666 (2006).
- 505 2. Myhre, G. *et al.* *Anthropogenic and natural radiative forcing. Climate Change 2013: The*
506 *Physical Science Basis. Contribution of Working Group I to the Fifth Assessment Report*
507 *of the Intergovernmental Panel on Climate Change* (Cambridge University Press, 2013).
- 508 3. Meehl, G. A., Arblaster, J. M. & Branstator, G. Mechanisms contributing to the warming
509 hole and the consequent US east–west differential of heat extremes. *J. Clim.* **25**, 6394–
510 6408 (2012).
- 511 4. Yu, S. *et al.* Attribution of the United States ‘warming hole’: Aerosol indirect effect and
512 precipitable water vapor. *Sci. Rep.* **4**, doi: 10.1038/srep06929 (2014).
- 513 5. Leibensperger, E. M. *et al.* Climatic effects of 1950–2050 changes in US anthropogenic
514 aerosols-Part 2: Climate response. *Atmos. Chem. Phys.* **12**, 3349–3362 (2012).
- 515 6. Leibensperger, E. M. *et al.* Climatic effects of 1950–2050 changes in US anthropogenic
516 aerosols-Part 1: Aerosol trends and radiative forcing. *Atmos. Chem. Phys.* **12**, 3333–3348

- 517 (2012).
- 518 7. Mascioli, N. R., Fiore, A. M., Previdi, M. & Correa, G. Temperature and Precipitation
519 Extremes in the United States: Quantifying the Responses to Anthropogenic Aerosols and
520 Greenhouse Gases. *J. Clim.* **29**, 2689–2701 (2016).
- 521 8. Chin, M. *et al.* Multi-decadal aerosol variations from 1980 to 2009: a perspective from
522 observations and a global model. *Atmos. Chem. Phys.* **14**, 3657–3690 (2014).
- 523 9. Hsu, N. C. *et al.* Global and regional trends of aerosol optical depth over land and ocean
524 using SeaWiFS measurements from 1997 to 2010. *Atmos. Chem. Phys.* **12**, 8037–8053
525 (2012).
- 526 10. Cherian, R., Quaas, J., Salzmann, M. & Wild, M. Pollution trends over Europe constrain
527 global aerosol forcing as simulated by climate models. *Geophys. Res. Lett.* **41**, 2176–2181
528 (2014).
- 529 11. Streets, D. G., Wu, Y. & Chin, M. Two-decadal aerosol trends as a likely explanation of
530 the global dimming/brightening transition. *Geophys. Res. Lett.* **33**, doi:
531 10.1029/2006GL026471 (2006).
- 532 12. Streets, D. G. *et al.* Anthropogenic and natural contributions to regional trends in aerosol
533 optical depth, 1980–2006. *J. Geophys. Res. Atmos.* **114**, doi: 10.1029/2008JD011624
534 (2009).
- 535 13. Keppel-Aleks, G. & Washenfelder, R. A. The effect of atmospheric sulfate reductions on
536 diffuse radiation and photosynthesis in the United States during 1995–2013. *Geophys.*
537 *Res. Lett.* **43**, 9984–9993 (2016).
- 538 14. Melillo, J. M., Richmond, T. T. & Yohe, G. *Climate change impacts in the United States:*
539 *Third National Climate Assessment. U.S. Global Change Research Program* (2014).

- 540 doi:10.7930/J0Z31WJ2
- 541 15. Karl, T. R., Knight, R. W., Easterling, D. R. & Quayle, R. G. Indices of climate change
542 for the United States. *Bull. Am. Meteorol. Soc.* **77**, 279–292 (1996).
- 543 16. Zhang, J. & Reid, J. S. An analysis of clear sky and contextual biases using an operational
544 over ocean MODIS aerosol product. *Geophys. Res. Lett.* **36**, doi: 10.1029/2009GL038723
545 (2009).
- 546 17. Buchard, V. *et al.* The MERRA-2 aerosol reanalysis, 1980 onward. Part II: Evaluation and
547 case studies. *J. Clim.* **30**, 6851–6872 (2017).
- 548 18. Randles, C. *et al.* The MERRA-2 aerosol reanalysis, 1980–onward. Part I: System
549 description and data assimilation evaluation. *J. Clim.* **30**, 6823–6850 (2017).
- 550 19. Seinfeld, J. H. & Pandis, S. N. *Atmospheric chemistry and physics: from air pollution to*
551 *climate change*. (John Wiley & Sons, 2006).
- 552 20. Fiore, A. M., Naik, V. & Leibensperger, E. M. Air quality and climate connections. *J. Air*
553 *Waste Manage. Assoc.* **65**, 645–685 (2015).
- 554 21. Holben, B. N. *et al.* AERONET—A federated instrument network and data archive for
555 aerosol characterization. *Remote Sens. Environ.* **66**, 1–16 (1998).
- 556 22. Moran, P. A. P. Notes on continuous stochastic phenomena. *Biometrika* **37**, 17–23 (1950).
- 557 23. Curran, P. J. The semivariogram in remote sensing: an introduction. *Remote Sens.*
558 *Environ.* **24**, 493–507 (1988).
- 559 24. Zhang, L. *et al.* What factors control the trend of increasing AAOD over the United States
560 in the last decade? *J. Geophys. Res. Atmos.* **122**, 1797–1810 (2017).
- 561 25. Buchard, V. *et al.* Using the OMI aerosol index and absorption aerosol optical depth to
562 evaluate the NASA MERRA Aerosol Reanalysis. *Atmos. Chem. Phys.* **15**, 5743–5760

- 563 (2015).
- 564 26. Dawson, J. P., Adams, P. J. & Pandis, S. N. Sensitivity of PM_{2.5} to climate in the Eastern
565 US: a modeling case study. *Atmos. Chem. Phys.* **7**, 4295–4309 (2007).
- 566 27. Paasonen, P. *et al.* Warming-induced increase in aerosol number concentration likely to
567 moderate climate change. *Nat. Geosci.* **6**, 438–442 (2013).
- 568 28. Megaritis, A. G., Fountoukis, C., Charalampidis, P. E., Pilinis, C. & Pandis, S. N.
569 Response of fine particulate matter concentrations to changes of emissions and
570 temperature in Europe. *Atmos. Chem. Phys.* **13**, 3423–3443 (2013).
- 571 29. Horton, D. E., Skinner, C. B., Singh, D. & Diffenbaugh, N. S. Occurrence and persistence
572 of future atmospheric stagnation events. *Nat. Clim. Chang.* **4**, 698–703 (2014).
- 573 30. Gkikas, A., Houssos, E. E., Hatzianastassiou, N., Papadimas, C. D. & Bartzokas, A.
574 Synoptic conditions favouring the occurrence of aerosol episodes over the broader
575 Mediterranean basin. *Q. J. R. Meteorol. Soc.* **138**, 932–949 (2012).
- 576 31. Tai, A. P. K. *et al.* Meteorological modes of variability for fine particulate matter (PM_{2.5})
577 air quality in the United States: implications for PM_{2.5} sensitivity to climate change.
578 *Atmos. Chem. Phys.* **12**, 3131–3145 (2012).
- 579 32. Pye, H. O. T. *et al.* Effect of changes in climate and emissions on future sulfate-nitrate-
580 ammonium aerosol levels in the United States. *J. Geophys. Res. Atmos.* **114**, doi:
581 10.1029/2008JD010701 (2009).
- 582 33. Dawson, J. P., Bloomer, B. J., Winner, D. A. & Weaver, C. P. Understanding the
583 meteorological drivers of US particulate matter concentrations in a changing climate. *Bull.*
584 *Am. Meteorol. Soc.* **95**, 521–532 (2014).
- 585 34. Brock, C. A. *et al.* Aerosol optical properties in the southeastern United States in summer–

- 586 Part 2: Sensitivity of aerosol optical depth to relative humidity and aerosol parameters.
587 *Atmos. Chem. Phys.* **16**, 5009–5019 (2016).
- 588 35. Hansen, J., Sato, M. & Ruedy, R. Perception of climate change. *Proc. Natl. Acad. Sci.*
589 **109**, E2415–E2423 (2012).
- 590 36. US Environmental Protection Agency. Air pollutant emissions trends data: State average
591 annual emissions trend. (2016). Available at:
592 https://www.epa.gov/sites/production/files/2016-12/state_tier1_90-16.xls. (Accessed: 7th
593 February 2017)
- 594 37. Takemura, T., Nakajima, T., Dubovik, O., Holben, B. N. & Kinne, S. Single-scattering
595 albedo and radiative forcing of various aerosol species with a global three-dimensional
596 model. *J. Clim.* **15**, 333–352 (2002).
- 597 38. Sasser, E. *et al.* Report to Congress on Black Carbon. Available at:
598 <https://www3.epa.gov/airquality/blackcarbon/>. EPA-450/R-12-001 (2012).
- 599 39. Hand, J. L., Schichtel, B. A., Pitchford, M., Malm, W. C. & Frank, N. H. Seasonal
600 composition of remote and urban fine particulate matter in the United States. *J. Geophys.*
601 *Res. Atmos.* **117**, doi: 10.1029/2011JD017122 (2012).
- 602 40. Ehn, M. *et al.* A large source of low-volatility secondary organic aerosol. *Nature* **506**,
603 476–479 (2014).
- 604 41. Teakles, A. D. *et al.* Impacts of the July 2012 Siberian fire plume on air quality in the
605 Pacific Northwest. *Atmos. Chem. Phys.* **17**, 2593–2611 (2017).
- 606 42. Levy, R. C. *et al.* Global evaluation of the Collection 5 MODIS dark-target aerosol
607 products over land. *Atmos. Chem. Phys.* **10**, 10399–10420 (2010).
- 608 43. Heidinger, A. K., Foster, M. J., Walther, A. & Zhao, X. The pathfinder atmospheres–

- 609 extended AVHRR climate dataset. *Bull. Am. Meteorol. Soc.* **95**, 909–922 (2014).
- 610 44. Kahn, R. A. *et al.* Multiangle Imaging Spectroradiometer (MISR) global aerosol optical
611 depth validation based on 2 years of coincident Aerosol Robotic Network (AERONET)
612 observations. *J. Geophys. Res. Atmos.* **110**, doi: 10.1029/2004JD004706 (2005).
- 613 45. McCarty, W. *et al.* in *Technical report series on global modeling and data assimilation*,
614 *Volume 46* (ed. Koster, R. D.) (2016). doi:20160014544
- 615 46. Rienecker, M. M. *et al.* MERRA: NASA’s Modern-Era Retrospective Analysis for
616 Research and Applications. *J. Clim.* **24**, 3624–3648 (2011).
- 617 47. Gelaro, R. *et al.* The Modern-Era Retrospective Analysis for Research and Applications,
618 Version 2 (MERRA-2). *J. Clim.* **30**, 5419–5454 (2017).
- 619 48. Giglio, L., Randerson, J. T. & Werf, G. R. Analysis of daily, monthly, and annual burned
620 area using the fourth-generation global fire emissions database (GFED4). *J. Geophys. Res.*
621 *Biogeosciences* **118**, 317–328 (2013).
- 622 49. Aneja, V. P., Nelson, D. R., Roelle, P. A., Walker, J. T. & Battye, W. Agricultural
623 ammonia emissions and ammonium concentrations associated with aerosols and
624 precipitation in the southeast United States. *J. Geophys. Res. Atmos.* **108**, doi:
625 10.1029/2002JD002271 (2003).
- 626 50. U.S. Environmental Protection Agency. in *Emission inventory improvement program*
627 (Available at: <https://www.epa.gov/sites/production/files/2015-08/documents/vi04.pdf>,
628 1996).
- 629 51. Fioletov, V. E., McLinden, C. A., Krotkov, N., Moran, M. D. & Yang, K. Estimation of
630 SO₂ emissions using OMI retrievals. *Geophys. Res. Lett.* **38**, doi: 10.1029/2011GL049402
631 (2011).

- 632 52. Levy, R. C. *et al.* A critical look at deriving monthly aerosol optical depth from satellite
633 data. *IEEE Trans. Geosci. Remote Sens.* **47**, 2942–2956 (2009).
- 634 53. Sullivan, R. C., Levy, R. C. & Pryor, S. C. Spatiotemporal coherence of mean and
635 extreme aerosol particle events over eastern North America as observed from satellite.
636 *Atmos. Environ.* **112**, 126–135 (2015).
- 637 54. Liebhold, A. M. & Sharov, A. A. in *Population and community ecology for insect*
638 *management and conservation* (ed. Baumgärtner, J., P. Brandmayr, and B. M.) 111–117
639 (Balkema, 1998).
- 640 55. Agresti, A. *Analysis of ordinal categorical data.* (John Wiley & Sons, 2010).
- 641 56. Wilks, D. S. *Statistical methods in the atmospheric sciences.* (Academic press, 2011).
- 642 57. Cattell, R. B. The scree test for the number of factors. *Multivariate Behav. Res.* **1**, 245–
643 276 (1966).
- 644 58. Richman, M. Rotation of principal components. *J. Climatol.* **6**, 293–335 (1986).

646 **6 Acknowledgements**

647 Funding was supplied by: NASA Earth and Space Science Fellowship Program - Grant
648 NNX14AP56H (RCS) and NASA (NNX16AG31G) (SCP and RCL). We acknowledge
649 computational resources provided by the Lilly Endowment, Inc. to the Indiana University
650 Pervasive Technology Institute and the Indiana METACyt Initiative, and thank the AERONET
651 PIs for establishing and maintaining the sites used herein.

652 **7 Contributions**

653 RCS and SCP jointly identified the research objectives and designed the research
654 methodology, RCS conducted the majority of the analyses, SCP analyzed the AERONET

655 observations, and SCP and RCS jointly wrote the manuscript. RCL and AMS provided expertise
656 on the MERRA-2 dataset, and discussed and commented on the manuscript.

657 **8 Competing interests**

658 The authors declare no competing interests.

659 **9 Figure legends**

660 Figure 1. The eight U.S. National Climate Assessment (NCA) regions in which the aerosol-CIs
661 are computed. The CIs are computed using MERRA-2 daily-averaged output from all
662 grid cells within the dashed lines enclosing each region. Note the Great Plains region has
663 been divided into two regions to ease interpretation of the analyses. Abbreviations: AK =
664 Alaska, NW = Northwest, SW = Southwest, GPu = upper Great Plains, GPl = lower
665 Great Plains, MW = Midwest, SE = Southeast, and NE = Northeast. Also shown within
666 the map are the locations of AERONET sites from which data are presented in Figure S1.
667 Figure was created using MATLAB (2016b; mathworks.com).

668 Figure 2. a and b) Mean (marker) and ± 1 standard deviation (whiskers) values of the aerosol-CIs
669 during the study period (2000 – 2015). Upward and downward facing triangles indicate
670 significant positive and negative trends as determined using Kendall's tau-b, while square
671 markers indicate no significant trend (at $\alpha=0.05$). c) Percentage change per year in the
672 CIs estimated using a linear regression fit (shown in Figures S2 and S3). The middle
673 circles denote the normalized regression slopes (i.e. trends), and the inner and outer
674 circles are the lower and upper bounds, respectively, of the 95% confidence intervals of
675 these slopes. Black circles indicate trends that are not significant at $\alpha=0.05$.

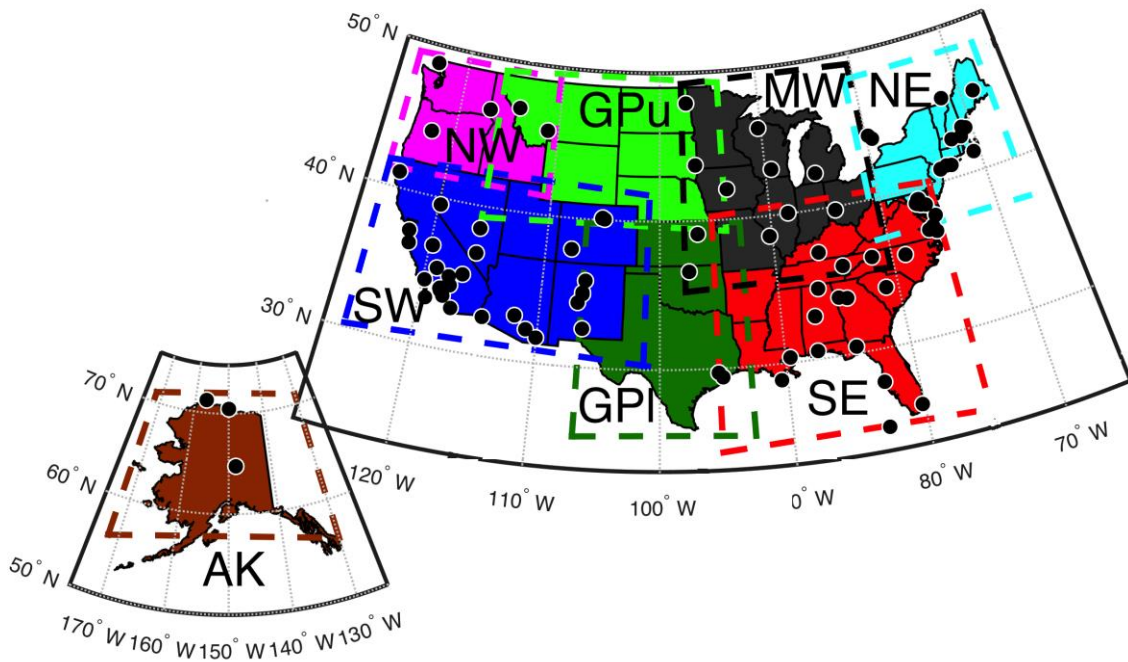
676 Figure 3. Cumulative distribution functions (cdf) of data from 2000 – 2015 for a) AOD, b) AE,
677 and c) SSA in each region. The cdf for all years is shown in black (labels under lower

678 panel), while the deviation from the mean is shown for each year with the color scheme
679 transitioning from blue (2000) to green (2015) (labels above top panel). d) Time series of
680 the yearly seasonal mean extreme AOD for each region. Significant trends in the daily
681 mean values are indicated by a red '+' or '-' in each panel (a-c) for positive and negative
682 trends, respectively, and to the right of each panel in (d).

683 Figure 4. Mean synoptic conditions for synoptic types associated with anomalously low and high
684 AOD for each region (locations shown in Figure 1). The mean temperature at 700 hPa (in
685 K) are shown by the background colors, the solid black lines depict the 500 hPa
686 geopotential isoheights (in m), and the red, magenta, cyan, and blue stippling represent
687 700 hPa specific humidity anomalies -2, -1, +1, and +2 standard deviations from the
688 mean for all days. The arrows beside the panels indicate the presence and direction of
689 significant trends in the PC scores associated with these synoptic types. The abscissa and
690 ordinate axes are longitude (degrees East) and latitude (degrees North), respectively.

691 Figure 5. a) Time series of annual anthropogenic emissions as reported in the U.S. EPA National
692 Emissions Inventory of carbon monoxide (CO), ammonia (NH₃), nitrogen oxides (NO_x),
693 particulate matter < 10 μm (PM₁₀), fine particulate matter < 2.5 μm (PM_{2.5}), sulfur
694 dioxide (SO₂), and volatile organic compounds (VOC) by region, in thousands of tons per
695 year³⁶. b) Time series of wildfire occurrence expressed as monthly burned area for each
696 region, derived from MODIS measurements⁴⁸. The sign of significant trends are shown
697 above each panel in a) and next to the legend in b) (*positive trend in NW monthly
698 burned area p-value = 0.13).

699

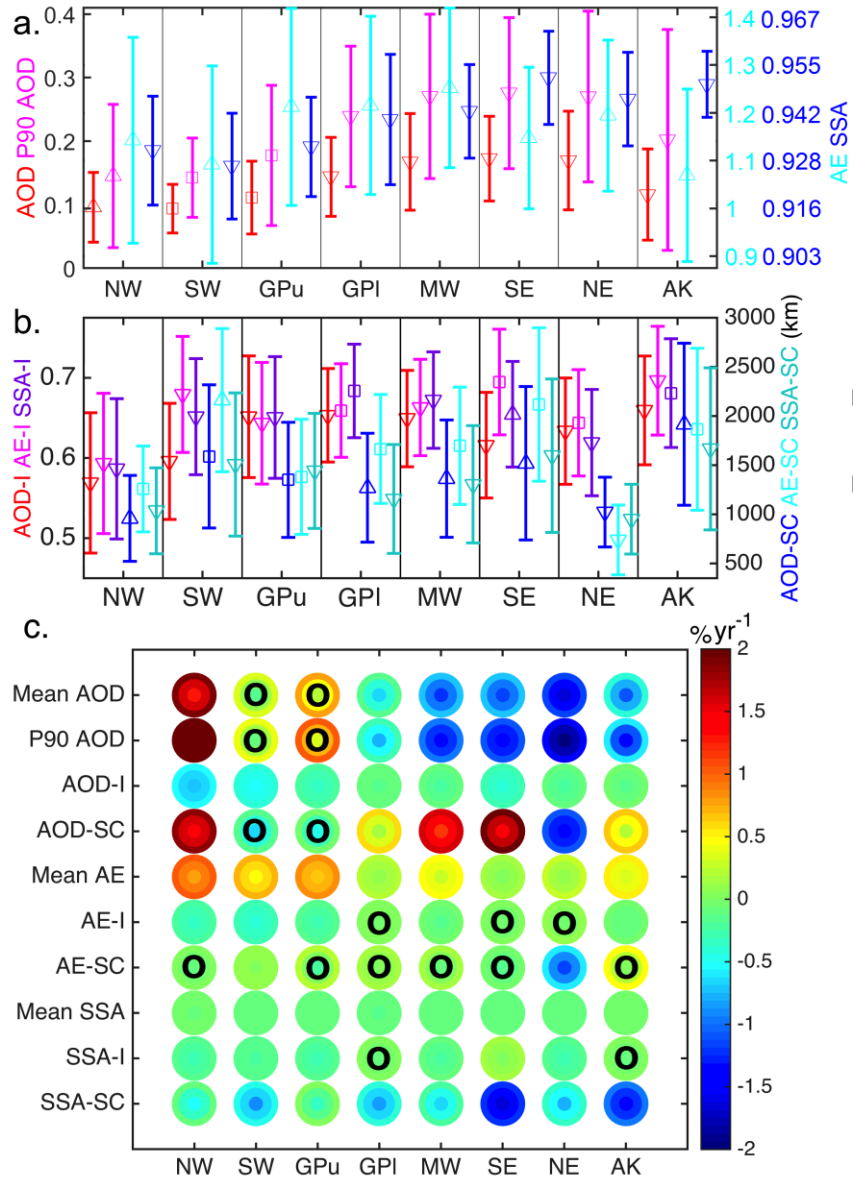


701

702

Figure 1.

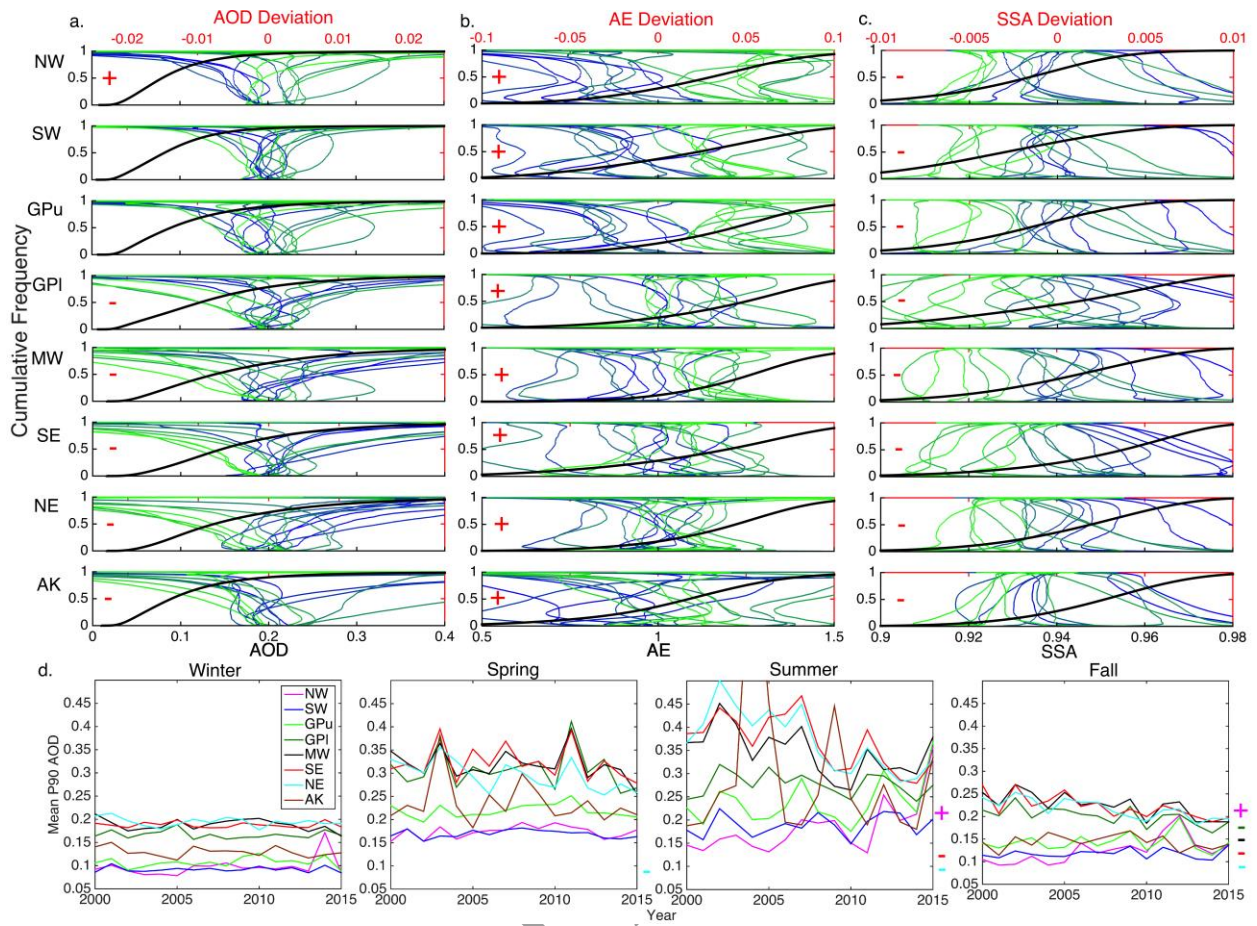
Accepted manuscript



703

704

Figure 2.



705

706

Accepted

Figure 3.

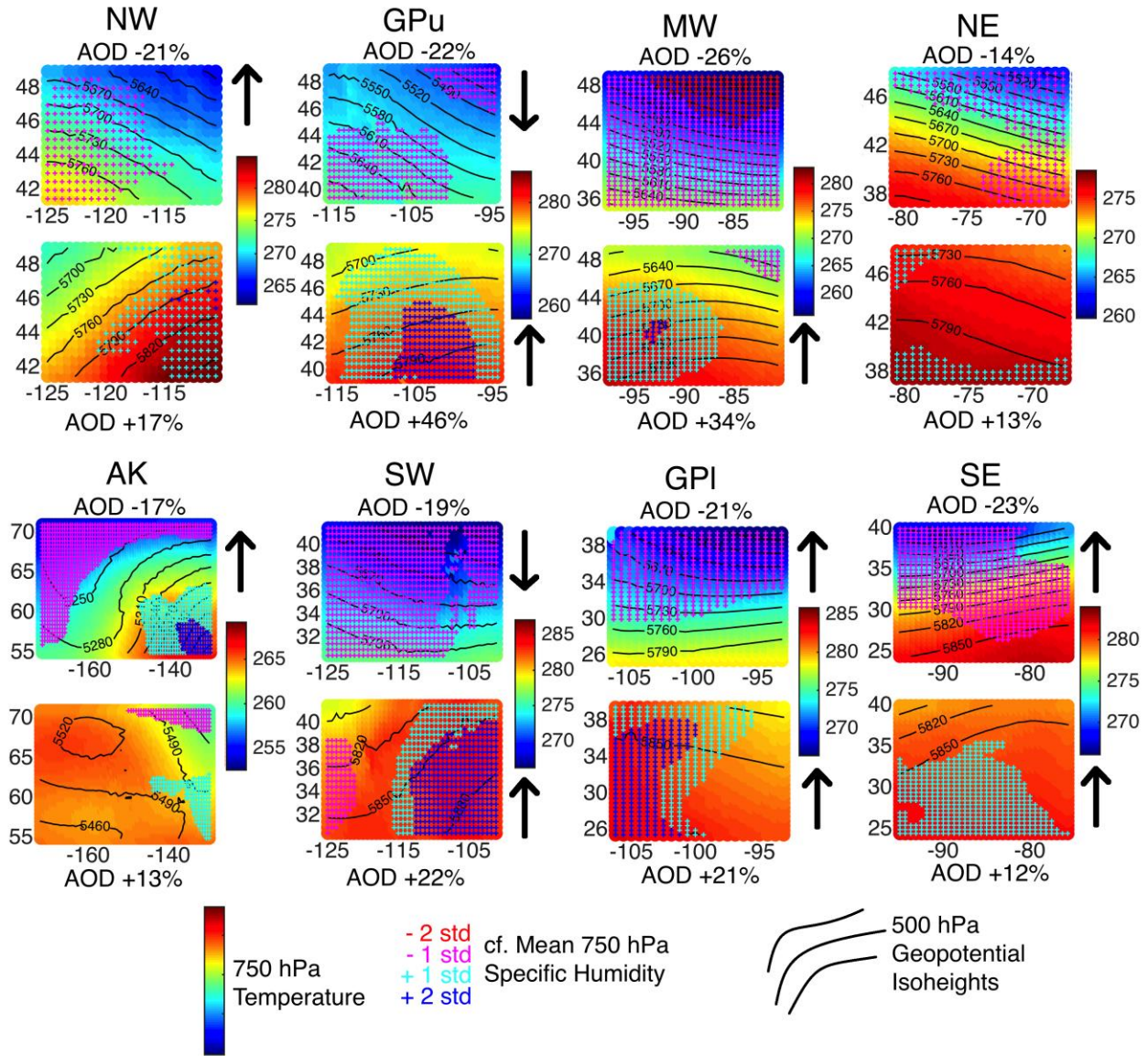


Figure 4.

707
708

ACCE

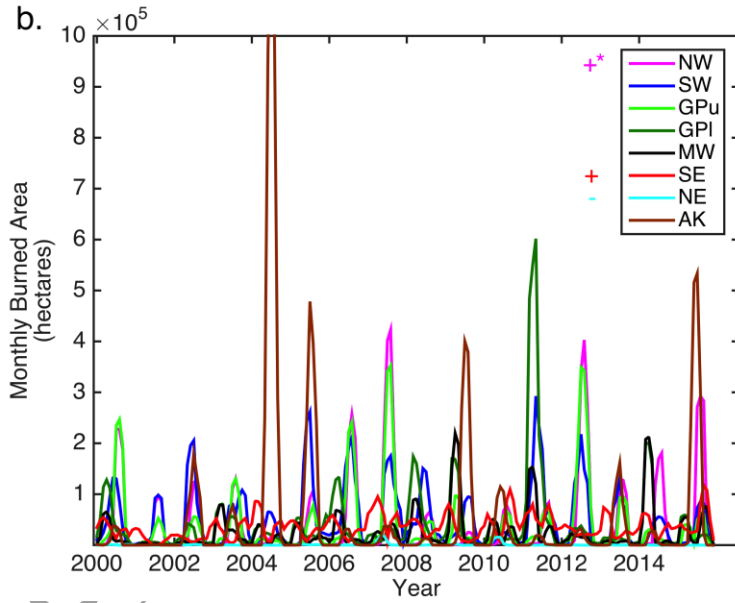
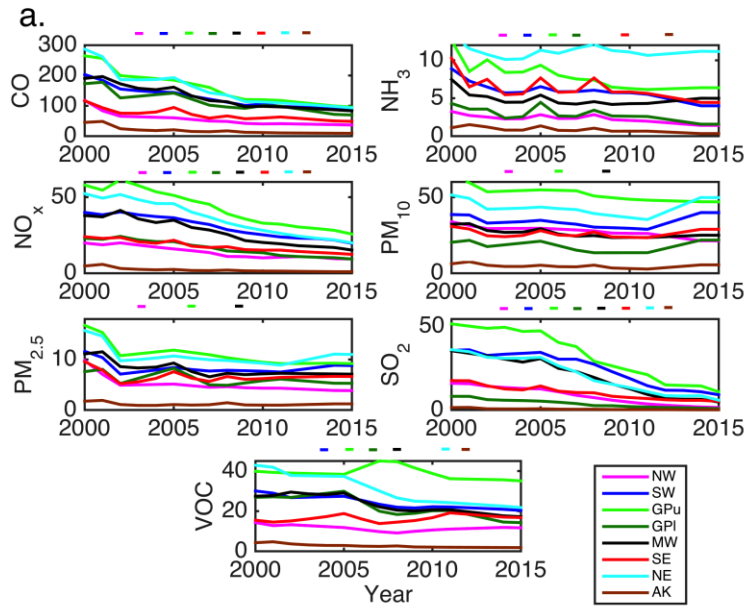


Figure 5.

709

710

711